Article

Influence of the heat treatment duration on the cycling performance and electrochemical mechanism of Na2Ti3O7 as anode material for Na-ion batteries

Caroline Piffet *, Nicolas Eshraghi, Gregory Mottet, Frédéric Hatert, Jolanta Swiatowska *, Rudi Cloots, Frederic Boschini, Abdelfattah Mahmoud *

Posted Date: 2 August 2023

doi: 10.20944/preprints202308.0060.v1

Keywords: Na-ion batteries; Na2Ti3O7; Operando XRD; Insertion mechanism; Electreochemical impedance spectroscopy

Preprints (www.preprints.org) | NOT PEER-REVIEWED | Posted: 2 August 2023 doi:10.20944/preprints202308.0060.v1

Article

Influence of the Heat Treatment Duration on the Cycling Performance and Electrochemical Mechanism of $Na_2Ti_3O_7$ as Anode Material for Na-Ion Batteries

Caroline Piffet [1,*], Nicolas Eshraghi [1,¥], Gregory Mottet [1], Frédéric Hatert [2], Jolanta Światowska [3,†], Rudi Cloots [1], Frédéric Boschini [1] and Abdelfattah Mahmoud [1,*]

[1] GREENMAT, CESAM Research Unit, Chemistry Department, University of Liège, 4000 Liège, Belgium.
[2] Laboratory of Mineralogy, Geology Research Unit, University of Liège, 4000 Liège, Belgium.
[3] Chimie ParisTech - CNRS, PSL University, Institut de Recherche de Chimie Paris, 75005 Paris, France
[*] Correspondence: authors: *caroline.piffet@uliege.be/*abdelfattah.mahmoud@uliege.be, Greenmat, University of Liège, Quartier Agora, Allée du 6 Août 13 Bat B6A, 4000 Liège (Belgium); +3243663543
[¥] Present address: Umicore, Umicore Research,Development & Innovation, 2250 Olen, Belgium
[†] jolanta.swiatowska@chimieparistech.psl.eu. Chimie ParisTech - CNRS, PSL University, Institut de Recherche de Chimie Paris, 75005 Paris, France.

Abstract: The growing interest in Na-ion batteries as a "beyond lithium" technologies for energy storage drives the research for high-performance and environment-friendly materials. $Na_2Ti_3O_7$ (NTO) as an eco-friendly, low-cost anode material shows a very low working potential of 0.3 V *vs* Na^+/Na but suffers from poor cycling stability, which properties can be significantly influenced by materials synthesis and treatment. Thus, in this work, the influence of the calcination time on the electrochemical performance and the reaction mechanism during cycling were investigated. NTO heat-treated for 48 h at 800 °C (NTO-48h) demonstrated enhanced cycling performance in comparison to NTO heat-treated for only 8 h (NTO-8h). The pristine material was thoroughully characterized by X-ray diffraction, laser granulometry, X-ray photoelectron spectroscopy, and specific surface area measurements. The reaction mechanisms induced by sodiation/desodiation and cycling were investigated by *opernado* XRD. Electrochemical impedance spectroscopy was used to evidence the evolution of the solid electrolyte interface layer (SEI) and modification of charge transfer resistances as well as the influence of cycling on capacity decay. The evolution of the crystallographic structure of NTO-48h revealed a more ordered structure and lower surface contamination compared to NTO-8h. Moreover, the residual $Na_4Ti_3O_7$ phase detected after the sodium extraction step in NTO-8h seems correlated to the lower electrochemical performance of NTO-8h compared to NTO-48h.

Keywords: Na-ion batteries; $Na_2Ti_3O_7$; *Operando* XRD; Insertion mechanism; electreochemical impedance spectroscopy

Highlights:

What are the main findings?

- NTO heat-treated 8 h has a less ordered structure and more surface contamination.
- After oxidation, some Na^+ ions are trapped in NTO heat-treated 8 h structure.

What is the implication of the main finding?

- The increase of the calcination time leads to higher electrochemical performance.
- The charge transfer resistance evolution in NTO depends on the reversible formation/deformation of $Na_4Ti_3O_7$ phase.
- The R_t evolution depends on the reversible formation/deformation of $Na_4Ti_3O_7$ phase.

1. Introduction

Due to the growing stress on the economic viability of Li-ion batteries as the dominant technology for energy storage devices, Na-ion batteries have emerged as a promising low-cost chemistry for energy storage. Indeed, sodium is a much more abundant element than lithium in Earth's crust. The lower energy density of Na is expected to mostly confine it to large-scale storage systems for grid storage applications [1–4]. To succeed in this transition, efficient electrode materials with high electrochemical performance need to be developed and their reaction mechanisms during the operation of the battery have to be well understood.

Right now the most common active anode materials for NIBs are hard carbons [5,6]. Despite these favorable properties, non-carbonaceous alternatives are also under investigation for cases where thermal stability is prioritized [7,8]. $Na_2Ti_3O_7$ (NTO) is considered as a promising anode material for Na-ion batteries due to its low working potential of 0.3V *vs* Na^+/Na [2,9] among intercalation oxide category materials. It can deliver theoretically 178 mAh/g with the intercalation of two additional sodium ions into its layer structure: $Na_2Ti_3O_7 + 2\ Na^+ + 2\ e^- \rightarrow Na_4Ti_3O_7$, so that 2/3 of the Ti^{4+} ions are reduced to Ti^{3+} ions [2,9,10]. Next to these advantages, NTO suffers from low electronic conductivity, limited cycling stability and poor capacity retention. These problems lead to a deterioration of the electrochemical performance [10–12].

As it was recently pointed by Kulova *et al.* [13], the origins of these problems are various and sometimes even contradictory. Wang *et al.* [14] reported that, even if the crystal structure of NTO is very stable, the cycle irreversibility could be related to problems of Na^+ extraction, then progressive saturation of interacalation sites by Na^+ ions until inhibition of ionic transport and migration. According to Rudola *et al.* [15], diffusion problems could explain the capacity drop at high cycling rates: due to kinetic limitation, Na^+ ions would have no time to intercalate/deintercalated into the structure of NTO. On the other hand, even if the delivered capacity of the material decreases with the increase of the cycling rate, Pan *et al.* [16] observed an increase of capacity fading at low current density because side reactions consuming large amounts of sodium have more time to occur. Incidental reactions with the carbon black [11,17,18] and/or with electrolyte [11,16,18,19] and/or binders [20] were also pointed as the origin of the first cycle irreversibility. Structural instability of the intercalated $Na_4Ti_3O_7$ phase was reported by Xu *et al.* [17]. By contrast, Nava-Avendaño *et al.* [11] confirmed the good mechanical stability of this phase and reported that the exchange of Na^+ by H^+ ions during electrode preparation or storage of NTO material had no negative effect on the electrochemical performance because the H^+ ions were further replaced by Na^+ ions from the electrolyte [11]. Pan *et al.* [16] evidenced the formation of an intermediate phase during sodium intercalation into the NTO structure. Two close voltage plateaus at 0.289 and 0.403 V were observed during the first charge process but the first plateau disappeared during the following cycles. By reducing the particles size with a ball-milling step, the formation of the intermediate phase was suppressed and the electrochemical performance improved. The formation of an intermediate phase during the first cycle was also largely discussed by Rudola *et al.* [21]. According to these authors, the pathway $Na_2Ti_3O_7 \leftrightarrow Na_{3-x}Ti_3O_7$ should be favored instead of the fully sodiated pathway $Na_2Ti_3O_7 \leftrightarrow Na_4Ti_3O_7$ because the polarization phenomena is alleviated, which leads to improved material stability and higher capacity retention.

In addition, the temperature of the heat treatment influences the crystallographic structure and purity of sodium titanates [15,22]. It should be noted that crystallographic structure and defects affect the electrochemical performance of NTO [23,24]. Moreover, both in the literature [25] and in our previous work [26], the higher capacities were dobtained by NTO synthesized at 1000 °C than at 800 °C. If the temperature of the heat treatment affects electrochemical performance [25–27], it can be expected that the duration of the heat treatment could also impact the electrochemical properties.

Here, the investgation of the effect of the heat-treatment conditions (8 h or 48 h at 800°C) on the electrochemical properties of the $Na_2Ti_3O_7$ anode material is presented. Indeed, new clarifications on the sodiation/desodiation mechanism in $Na_2Ti_3O_7$ induced by cycling in half-cell configuration, using *operando* XRD are demonstrated. Although a few previous works by *in situ* [2,25] or *exsitu* XRD [21] already shown the charge/discharge process in NTO, we provide new insights in different electrochemical performances of NTO influenced by cycling and heat treatment durations (8 h and

doi:10.20944/preprints202308.0060.v1

48 h). The *operando* XRD measurements are complemented by other characterization results by means of *ex situ* XRD, XPS, laser granulometry, BET specific surface area, scanning electron microscopy, cyclic voltammetry and galvanostatic cycling) aiming at a comprehensive and complete view of the structural, morphological, surface and electrochemical properties.

2. Materials and Methods

2.1. Materials

TiO_2 (Degussa P25, 99.5+ %), Duramax D-3005 (ammonium salt of a polyelectrolyte, dispersing agent kindly provided by Dow Chemical), Na_2CO_3 (Sigma Aldrich), carbon black (Alpha Aesar, 50% compressed), multiwall carbon nanotubes (CNT, 3 wt % dispersion ORGACYL™ NMP0502 (Nanocyl), N-methyl-2-pyrrolidone (NMP, Sigma Aldrich), polyvinylidene fluoride (PVDF, Sigma Aldrich), $NaClO_4$ (Sigma Aldrich), propylene carbonate (PC, Sigma Aldrich) and ethylene carbonate (EC, Sigma Aldrich) were used as received.

2.2. Synthesis

An aqueous suspension containing the TiO_2 (10 wt %) and Na_2CO_3 precursors in a stoichiometric ratio was prepared as described in our previous work [26]. The spray-drying synthesis step was carried out in the air using a Niro Mobile Minor spray-dryer with bifluid nozzle. The inlet temperature was set at 190 °C to target an outlet temperature of 110-120 °C. The flow rate was set at 25 mL/min and the air pressure at 1 bar. The as-sprayed powders were then heated at 800 °C for 8 h (NTO-8h) or 48 h (NTO-48h).

2.3. Characterization

2.3.1. Structure Characterization by XRD

The structural properties of the $Na_2Ti_3O_7$ powders of samples NTO-8h and NTO-48h were investigated by powder XRD technique. The samples were deposited on a zero-background silicon sample holder and then inserted in a Bruker D8-Eco diffractometer equipped with a copper X-ray tube (CuKα radiation wavelength = 1.5418 Å). The radiation was filtered with a Ni filter, in order to completely remove the K_{beta} contribution. Scans in the range of 10 to 100° 2θ, with a step of 0.02° 2θ, and with a counting time of 10 s/step, were realized. The Bruker software TOPAS 4.2 was then used to perform the Rietveld refinement of the XRD patterns. Experimental details concerning the refinements are given in Table S1. Starting atomic coordinates, unit-cell parameters, and space group, were those from Yakubovich & Kireev [28]. After the refinement of experimental parameters (scale factor, unit-cell parameters, background, zero-point, sample displacement, absorption, roughness, FWHM, profile, and preferred orientation), atomic coordinates were released carefully, and the site occupancy factors for Ti and Na atoms were refined. Displacement parameters were constrained to 1 for all atoms.

2.3.2. Particles Size and Morphology

Particle size and morphological properties were evaluated by laser granulometry (Malvern Mastersizer 2000 Hydro) and scanning electron microscopy (ESEM Philips XL-30 at 15 kV). The BET specific surface area was determined from N_2 sorption isotherms measured at 77 K for relative pressure P/P^0 between 0 and 0.3 with a Micromeritics Asap 2020 Plus instrument. Degassing was applied for 180 min at 150 °C with a heating ramp of 10 °C/min. The Rouquerol criteria were used to select the pressure range used to estimate the BET surface [29] and set the pressure range under N_2 from 0 to 0.3 with a 0.03 step.

2.3.3. Surface Chemical Characterization XPS

X-ray photoelectron spectroscopy analysis was performed using an XPS Thermo Electron Escalab 250 spectrometer operating at 2 x 10^{-9} mbar vacuum during analysis. The spectrometer was calibrated with Au 4f7/2 at 84.1 eV. A monochromatic, micro-focusing, Al Kα X-ray source (hν = 1486.6 eV) was used. All analyses were conducted with a 500-µm X-ray spot size beam with a take-off angle of 90° to the sample surface. The survey spectra were performed with a pass energy of 100 eV and high-resolution core level spectra (Ti 2p, O 1s, Na 1s, C 1s) with a pass energy of 20 eV. The spectra fitting was performed using the AvantageTM software (Thermo ElectronCorp.). For the peak fitting a Shirley type background and Lorentzian/Gaussian 30/70 peak shape was applied.

2.3.4. Cell Preparation and Electrochemical Tests

The working electrode was prepared by dispersing NTO, CNT, and PVDF binder in NMP solvent (NTO:C:PVDF = 70:20:10 wt.) with planetary miller Retsch PM400/2 using zirconia balls with a diameter of 1.5 mm at 400 rpm during 20 min and then at 250 rpm during 60 min. The slurry was tape-casted (Byko-drive XL, V) on copper foil and dried at 110 °C for 12h under the vacuum to remove the solvent.

Metallic Na was used as a reference and counter electrode. The electrolyte consists of a 1 M solution of $NaClO_4$ in a mixture of PC:EC (v:v = 1:1) solvent and glass fiber Whatman was used as a separator. Electrochemical measurements were performed in coin cell configuration (2032) with a multichannel BTS Neware Potentiostat (cycling) and a multichannel BioLogic VMP3 Potentiostat (cyclic voltammetry) in a voltage window of 0.05-1.5 V *vs* Na^+/Na.

2.3.5. Operando X-ray Diffraction

The working electrode was prepared by dispersing NTO and carbon black powders in an agate mortar. Electrochemical *operando* XRD was performed in Bragg-Brentano geometry using a Bruker D8 Twin-Twin diffractometer with Cu K_{alpha} radiation and Lynxeye XET 1D-detector. A specific cell with a beryllium window was used as described by Leriche *et al.* [30]. XRD data were collected in the 10-48° 2θ-range with a 0.02° step-size and a 1.8 s/strip steptime. A full XRD scan was collected in 1 h, while the cycling of the material was performed at a rate of C/20. For the Rietveld refinement, the XRD patterns were fitted using the TOPAS software by applying the fundamental parameters approach to model the instrumental contribution. The structural model was taken from the PDF4+ database (# 04-015-7486) [28]. Occupation factors were fitted for sodium sites and fixed titanium and oxygen sites. It should be noted that due to the low resolution of the *operando* XRD patterns, the plots of the site occupation factors (SOF) of sodium were used to show trends.

2.3.6. Electrochemical Impedance Spectroscopy (EIS)

EIS measurements were performed at room temperature in three-electrode Swagelok configuration with NTO-8h and NTO-48h electrodes and metallic Na as a reference and counter electrode using a Biologic VMP3. EIS measurements were obtained in a frequency range from 1 MHz to 10 mHz (6 points per decade) at OCV and different voltages in discharge and charge for the first and second cycles.

3. Results and Discussion

3.1. Structural Properties of the NTO Pristine Materials

The structural analysis of the pristine NTO-8h (Figure S1) and NTO-48h (Figure S2) samples was performed by XRD using the Rietveld refinement method. The final R_{Bragg} values were 5.32 % and 3.92 % for NTO-8h and NTO-48h samples, respectively (Table S1). The atomic coordinates, temperature factors, site occupancies, and selected bond distances are summarized in Table S2 and Table S3. The structure model for NTO-48h sample fits better than for NTO-8h, as shown by lower R_{Bragg} values and lower standard deviations for all parameters (Table S1, Table S2, and Table S3). The $Na_2Ti_3O_7$ structure is similar to those described by Andersson & Wadsley (JCPDS # 04-009-3663) [31]

doi:10.20944/preprints202308.0060.v1

and by Yakubovich & Kireev (JCPDS # 04-015-7486) [28]. It consists of edge-sharing TiO_6 octahedra forming ribbons aligned along the *b* axis (Figure 1a). These zig-zag ribbons show three octahedra of width, which are connected to adjacent ribbons by sharing octahedral corners. These connected ribbons form octahedral kinked sheets align parallel to the (001) plane (Figure 1b).

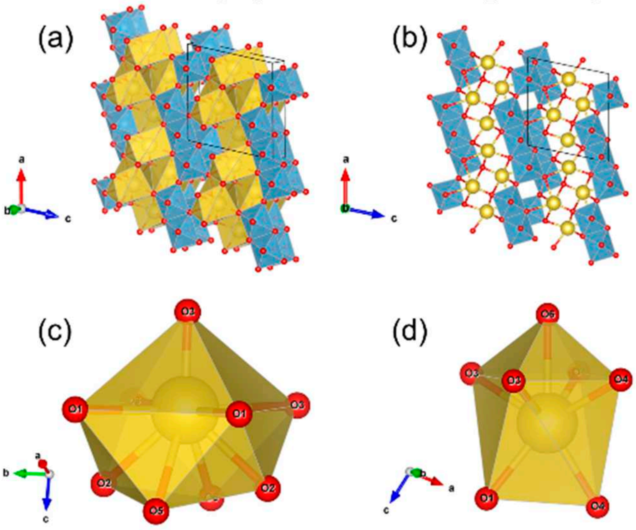

Figure 1. The crystal structure of $Na_2Ti_3O_7$ (sample NTO-8h). (a) Parallel projection to the ac plane, TiO_6 octahedra are in blue and NaOx polyhedra in yellow. (b) Parallel tprojection to the *ac* plane, TiO_6 octahedra are in blue and sodium atoms are shown as yellow spheres; the octahedral ribbons connected by corner-sharing to form planes parallel to (001) are visible. (c) Geometry of the $Na1O_9$ polyhedra and (d) the $Na2O_7$ polyhedra.

Between the octahedral Ti-bearing sheets, the Na atoms are localized in two types of crystallographic sites: the $Na1O_9$ site (Figure 1c) and the $Na2O_7$ site (Figure 1c). The $Na1O_9$ polyhedron geometry is quite complex, which can be described as a square pyramid with four supplementary oxygen localized at the opposite of the pyramid apex (Figure 1c). The $Na2O_7$ polyhedron corresponds to a square pyramid with its square face adjusted on the square face of a trigonal prism (Figure 1d).

Bond-valence sums were calculated according to the parameters of Brown & Altermatt [32], and indicate values close to 4 for Ti and to 1 for Na atoms (Table S3). This confirms the cation distributions, as well as the valence state of Ti. The bond-valence sum for Na2 is significantly lower than that of Na1 (Table S3), confirming the lower site occupancy factor of Na2 (Table S2). Bond-valence sums for oxygen atoms are between 1.83 and 2.12 (NTO-8h) and between 1.72 and 2.13 (NTO-48h), in good agreement with the valence of oxygen. The site occupancy factors for Na1, Ti1, Ti2, and Ti3 for NTO-48h, are close to 1, confirming the distributions of these cations in the crystal structure (Table S2).

As described by Papp et *al*. [22], the temperature of the heat treatment influenced the crystallographic structure of sodium titanates. Moreover, Rudola *et al.* [15] observed a decrease in the purity of $Na_2Ti_3O_7$ material while increasing the heat treatment from 10 h to 20 h and from 10 h to 40 h, at 800 °C, depending on the sodium precursor. By extension, the duration of the heat treatment could impact the structure and the purity of the material prepared in this work.

Yakubovich & Kireev [32] described in detail the distortion of the TiO_6 octahedra in the $Na_2Ti_3O_7$ structure. The authors explain that, due to the very dense packing of TiO_6 octahedra, a relatively strong distortion appears, mainly of the $Ti2O_6$ and $Ti3O_6$ polyhedra. In these polyhedra, a very short titanyl bond occurs, with a Ti-O distance around 1.70-1.75 Å. At the opposite, a very long bond forms with Ti-O around 2.18-2.25 Å. In the investigated compounds herein, the differences between Ti-O bond distances are less pronounced, leading to octahedral, and not pyramidal, coordination polyhedra.

In order to better evaluate the polyhedral distortion, bond-length distortion coefficients (BLD) were calculated according to the method established by Renner & Lehmann [32]. BLD coefficients are between 4.4 and 6.5 % for TiO_6 octahedra, indicating a global low distortion for these sites (Table S3). $Ti1O_6$ shows distortion coefficients of 6.47% (NTO-8h) and 6.01% (NTO-48h), significantly higher than the BLD values for $Ti2O_6$ and $Ti3O_6$ polyhedra (Table S3). This observation is in contradiction with Yakubovich & Kireev [28], who demonstrated that the $Ti1O_6$ octahedra is more distorted than the $Ti2O_6$ and $Ti3O_6$ octahedra.

Concerning the sodium sites, BLD coefficients indicate that the $Na1O_9$ site is strongly distorted, with values of 7.37 (NTO-8h) and 7.50 % (NTO-48h), while the $Na2O_7$ site is less distorted, with BLD values of 2.85% (NTO-8h) and 2.90 % (NTO-48h) (Table S3).

A comparison of the distortion coefficients, between the two samples, indicates that the sodium sites do not show significant variations in their distortion with the increase of the calcination duration. On the contrary, the TiO_6 octahedra are significantly less distorted when the synthesis duration increases (Table S3). These observations indicate that: (1) the increase of the synthesis duration leads to ordered structure, with less distorted coordination polyhedra, and (2) the distortion of framework TiO_6 polyhedra is more affected by modifications of the synthesis conditions than the extra-framework NaO_x polyhedra.

3.2. Microstructure of the Raw Materials

Scanning electron microscopy was used to determine the morphological properties of the NTO particles for both samples. It can be observed that NTO particles are rod- and platelet-like shape particles in the size range of 0.1-0.8 μm width and 0.1-5 μm length regardless of the heat treatment time (Figure 2a-d). These primary particles are agglomerated forming spheres due to the spray-drying process. These results are similar to the NTO spray-drying synthesis process reported by Zou *et al.* [18]. Nevertheless, that work described severe particles aggregation and broken spray-dried spheres when increasing the heating time from 5 h to 10 h at 800 °C. No aggregation is observed when increasing the heating time to 48 h for NTO-48h material produced in this study (Figure 2c-d).

The laser granulometry measurements provided complete particle size distribution (Figure 2e) of the spray-dried sphere, after heat-treatment. The $d_{0.5}$ value is 7.2 μm for NTO-8h and 6.1 μm for NTO-48h. This slight difference is probably due to the sintering effect, enhanced for NTO-48h due to the longer heat treatment duration. The specific surface area measured by BET is equal to 4.28 m^2/g (NTO-8h) and 3.64 m^2/g (NTO-48h). NTO-48h shows a little lower specific surface area probably due to shrinkage. Nevertheless, during the electrode preparation, the spheres will be grounded (deagglomeration of the primary particles) to increase the specific surface area and ensure a better contact with the electrolyte, leading to enhanced ionic diffusion.

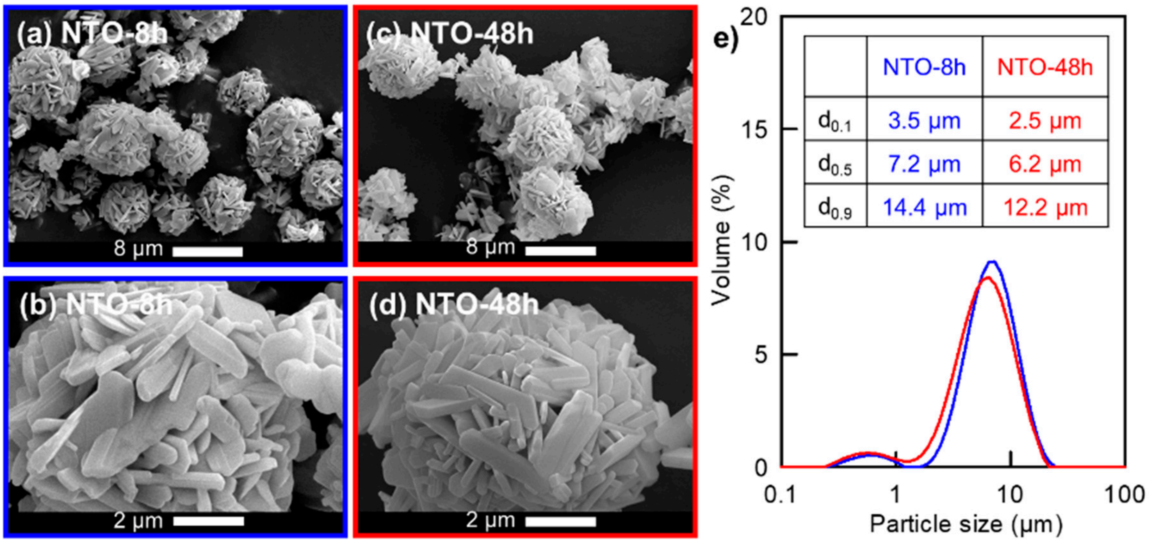

	NTO-8h	NTO-48h
$d_{0.1}$	3.5 μm	2.5 μm
$d_{0.5}$	7.2 μm	6.2 μm
$d_{0.9}$	14.4 μm	12.2 μm

doi:10.20944/preprints202308.0060.v1

Figure 2. SEM micrographs of $Na_2Ti_3O_7$ synthesized by spray-drying followed by a heat treatment at 800 °C for (a-b) 8 h or (c-d) 48 h. (e) Laser granulometry size distribution of NTO-8h (blue curve) and NTO-48h (red curve).

3.3. Chemical Characterisation by XPS

The surface chemical characterisation of the pristine NTO-8h and NTO-48h were performed by XPS and the spectra (Ti 2p, O 1s and Na 1s) are presented in Figure 3. For Ti, spin-orbit components (Ti $2p_{3/2}$ and Ti $2p_{1/3}$) with a splitting value of 5.7 eV are present (Figure 3a-b). The Ti $2p_{3/2}$ peak at binding energy of 458.2 eV indicates the presence of Ti^{4+} [33–35], which is in agreement with the existence of Ti^{4+} in $Na_2Ti_3O_7$ as demonsytrated by previous XPS on the NTO material. [15,36]

Similar shapes of Na 1s peaks at 1472.3 eV are observed for both samples. However, it should be noted that the Na 1s peak is overlapped with the Ti LMM Auger peaks at the lowest and the highest binding energies (as shown in Figure 3f). The modified Auger parameter for Na was determined from the energy shift between the Na 1s photoelectron line and the Na $KL_{23}L_{23}$ Auger line ($\alpha' = KE_{NaKL23L23} + BE_{Na\ 1s} = (h\nu - BE_{NaKL23L23}) + BE_{Na\ 1s}$). The kinetic energy of Na $KL_{23}L_{23}$ was similar for both samples of around 990.9 eV. Similar modified Auger parameter for both samples of 2062.2 eV indicates the presence of the same chemical state of sodium in $Na_2Ti_3O_7$ [37,38].

Both samples display also similar shapes of O 1s spectra. Four O 1s peaks can be distinguished: the first one at 529.7 eV attributed to Ti-O bonding, the higher binding energy peak at 531.6 eV corresponding to OH− (hydroxyl group) and C−O bond, the third one at 533.4 eV assigned to O−C=O species, and the highest binding energy peak at 534.9 eV assigned to Na KLL Auger line [33–35]. The presence of C-O related species originates from organic, surface contaminations usually present on sample surfaces exposed to the ambient air. Their presence can be also confirmed from the decomposition of C 1s peak (not shown here). Thus, from a decomposition of O 1s peaks and C 1s, the lower quantity of surface contamination can be observed for sample NTO-48h than for NTO-8h. Moreover, higher discrepancies in stoichiometry of O/Ti and O/Na on the surface of NTO-8h was also observed indicating some deficiencies in oxygen in $Na_2Ti_3O_7$.

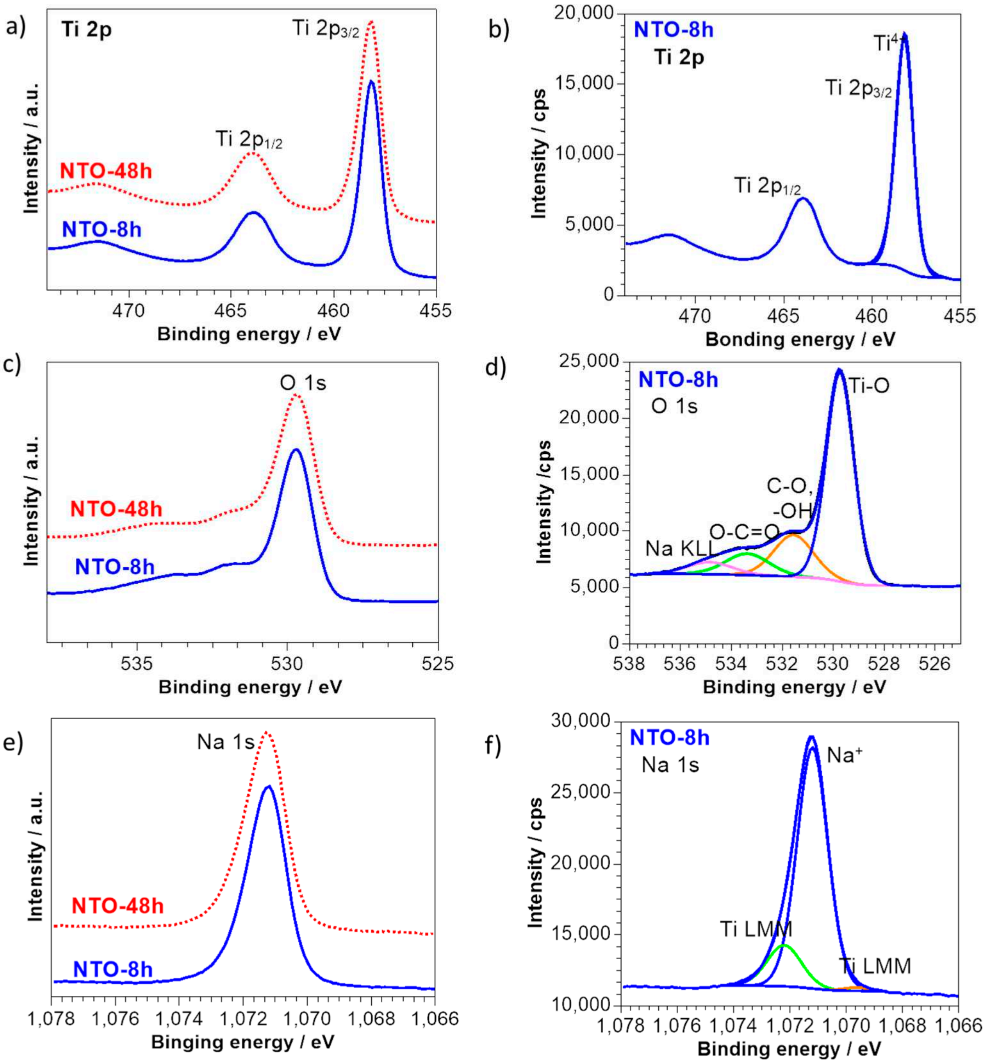

Figure 3. Comparison of XPS (a) Ti 2p, (c) O 1s and (e) Na 1s spectra obtained for NTO-8h and NTO-48h samples. Figures (b), (d), (f) show a decomposition of Ti 2p, O 1s and Na 1s, respectively, for NTO-8h sample.

3.4. Electrochemical Properties

3.4.1. Cyclic Voltammetry

To gain insight into the electrochemical behavior of NTO-8h and NTO-48h as anode materials, cyclic voltammetry was carried out in the voltage range of 0.05-1.5 V *vs* Na^+/Na (Figure 4a-b). The general shape of the CV curves is comparable to results reported in several previous studies [13,16,18,39]. During the first reduction process (red), two peaks corresponding to Na^+ insertion at 0.10 and 0.05 V for NTO-8h and at 0.09 and 0.05 V for NTO-48h which is consistent with the literature [13]. The additional reduction peak at higher voltage of 0.41 V (NTO-8h) or 0.38 V (NTO-48h) is attributed to the formation of SEI (Solid Electrolyte Interface) and side reactions with carbon black [2,13,15,18,19]. During the next cycles, the reduction peak corresponding to the SEI layer formation and side reactions is not anymore observed and the Na^+ insertion peaks at 0.05 V and 0.17 V can be still present. These results are very similar to the results of Kulova *et al.* [13], who also showed two peaks of sodiation at 0.04 and 0.12 V.

By contrast, the oxidation process for NTO-8h is very different than for NTO-48h. For NTO-8h, at the first cycle, oxidation occurrs in three steps: 0.30 V, 0.38 V, and 0.46 V. The previous investigations [13] reported the presense one peak at 0.33 V, which was described as a superposition of two or three peaks. In this study, the peak at 0.30 V is more intense than the other peaks and decreases gradually during the following cycles. The second peak at 0.36 V seems to disappear progressively in favor of the peak at 0.45 V up to complete extinction at the fourth cycle. According to the literature, this phenomenon can be related to the irreversibility of Na^+ extraction process but also to the structural evolution and phase modifications [13,15].

For NTO-48h, at the first cycle only two peaks are noticeable at 0.31 and 0.40 V. As for NTO-8h, the intensity of the first peak diminished progressively over the cycles. At the second cycle, the peak at 0.40 V vanished and another one appeared at 0.45 V. The third cycle (in blue) is different because a new peak at 0.37 V (not well marked, as for NTO-8h) appereas. The intensity of these two new peaks increases gradually in the fourth and fifth cycles. This result is similar to the observations of Rudola *et al.* [15], where the oxidation peak at 0.28 V decreased, while the intensity of the one at 0.44 V increased. These phenomena could be related to structural changes during electrochemical cycling [16] but also to the multi-step sodium insertion/extraction process that implies the formation of an intermediate phase $Na_{4-x}Ti_3O_7$ [13,21]. This will be further discussed in Section 3.4.4.

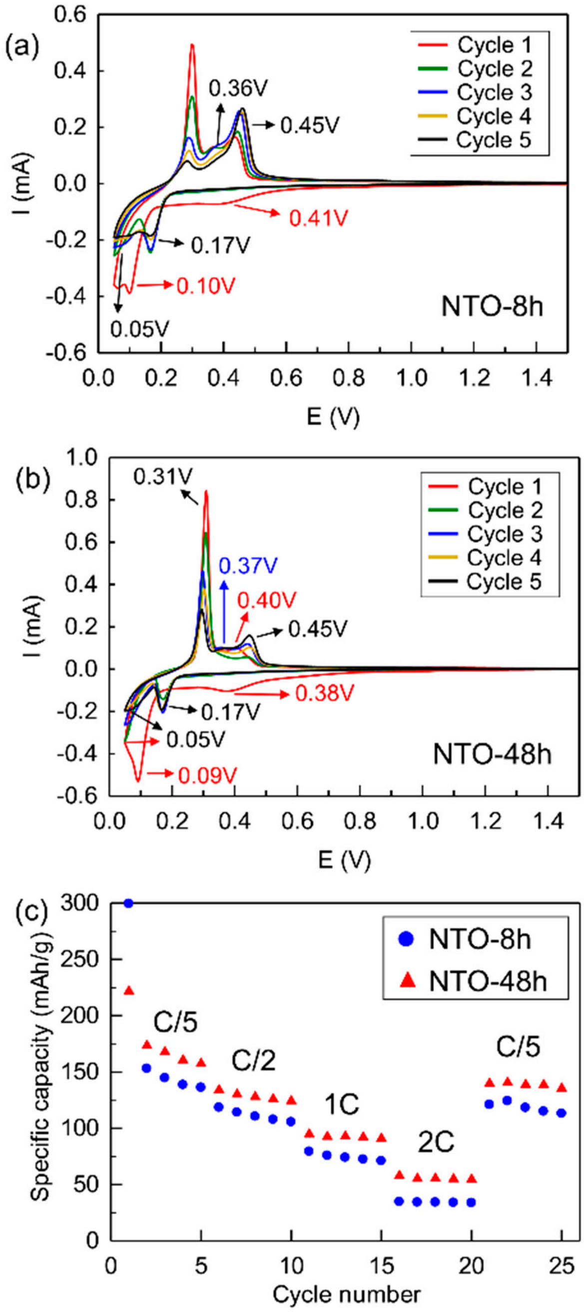

Figure 4. Cyclic voltammetry (0.05-1.5 V *vs* Na^+/Na with a scan rate of 0.1 mV/s) of (a) NTO-8h and (b) NTO-48h. (c) Rate capability at indicated cycling rate of NTO-8h and NTO-48h. Voltage window: 0.05-1.5 V *vs* Na^+/Na.

3.4.2. Galvanostatic Cycling

The electrochemical performance at different cycling rates (from C/5 to 2C) of NTO-8h and NTO-48h was evaluated within a voltage window of 0.05-1.5 V *vs* Na^+/Na (Figure 4c). The firs discharge capacity is very high 299 mAh/g for NTO-8h and 222 mAh/g for NTO-48h then decreases significantly during the following cycles. This very high initial capacity can be attributed to the SEI formation, as previously mentioned. However, it seems that less side reactions occurred during this first cycle for NTO-48h material, as the lower intitial capacity is than for NTO-8h. This could be related to the difference in surface chemistry and/or surface reactivity between both samples. Indeed, XPS measurements demonstrated less surface contaminations for NTO-48h.

The capacity loss between the first and the second cycle was much more important for NTO-8h (48.6%) than for NTO-48h (21.8%). This capacity decrease is well-known for NTO electrodes and usulally reported principal reasons are the side reactions with carbon black and the formation of an unstable SEI layer [11,13,15,18,19]. Kulova *et al.* [13] also mention that the alteration of the particles could be caused by their splitting during cycling. When increasing the cycling rate, NTO-48h still exhibits the higher capacities than NTO-8h. Indeed, the capacities at the second cycle (at indicated cycling rate) are 173 and 153 mAh/g (C/5), 130 and 114 mAh/g (C/2), 93 and 76 mAh/g (1C), 55 and 34 mAh/g (2C) for NTO-8h and NTO-48h, respectively.

The corresponding voltage profiles were very analogous for both calcination times (Figure 5 a, c). Three plateaus are observed during the first discharge (red curves). The first one at about 0.50 V is attributed to the SEI layer formation and side reactions occurring with carbon black [11,13,15,18,19,40]. This phenomenon is not visible anymore in the subsequent cycles, which agrees with the CV results presented above. Then, looking at lower potential, Na^+ ions undergo the insertion in two step-process: at about 0.20 and 0.10 V, in agreement with previous works on NTO anode [13,39,40].

For NTO-8h, the following discharge curves display only one plateau at about 0.20 V (Figure 5 a, c). This also agrees with studies of Kulova *et al.* [13] and Bhardwaj *et al.* [39], in which this behavior was attributed to instability and structural changes of the material during cycling. According to the work of Rudola *et al.* [21], this could also imply a mechanism with different pathways for the sodium insertion/extraction, i.e., a multi-step mechanism. By contrast, for NTO-48h, the other discharge curves still exhibit two plateaus for Na^+ ions extraction.

A two-step process can be observed for both samples at the charge rate of C/5: a short plateau at 0.30 V and a longer one at 0.40 V (Figure 5a,c), corresponding to the sodium extraction from the NTO materials.

At higher cycling rate, the discharge curves (Figure 5b,d, second cycle at the indicated rate) show less horizontal (flat) insertion plateaus. Kulova *et al.* [13] attributed these phenomena to the presence of a non-equilibrium solid solution at the surface of the NTO particles that can lead to the increased resistance at the surface of the electrode material and the polarization of the electrode. It was also reported that the cycling rate directly influenced the electrochemical phenomena within NTO material [13] and it was also observed for Li-ion batteries [41,42].

Further differences between NTO-8h and NTO-48h during sodium insertion were observed. For NTO-8h at the discharges of C/2, 1C and 2C rates one plateau at 0.2 V (Figure 5b) can be observed, while NTO-48h displays two plateaus for Na^+ extraction at 0.2 and 0.1 V (Figure 5d). Charge curves show two sodium extraction plateaus for both materials (Figure 5b, d): a first very short plateau at about 0.3 V and a second longer one at about 0.4 V. Polarization effect increases with the cycling rate.

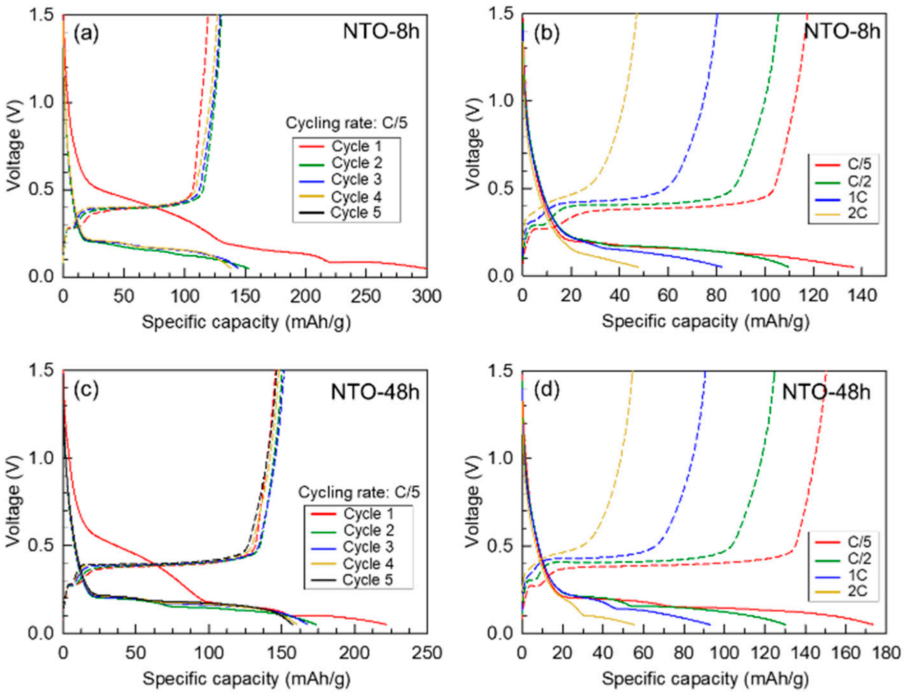

Figure 5. Electrochemical curves of (a-b) NTO-8h and (c-d) NTO-48h. Voltage window: 0.05-1.5 V *vs* Na+/Na. (a) and (c) First five cycles at C/5 cycling rate. (b) and (d) Second cycle at indicated cycling rate.

The difference in electrochemical behavior between NTO-8h and NTO-48h is discussed in more detail in Section 3.4.3 presenting *operando* XRD analyses and Section 3.4.4 presenting the EIS analyses.

For the long-term cycling at 1C rate (Figure 6), the NTO-48h material delivers higher capacities than NTO-8h material, over the 400 cycles. Moreover, the fluctuations of the capacity values are similar to the results of Bhardwaj *et al.* [39].

One reason for the higher electrochemical performance of NTO-48h compared to NTO-8h during the rate capability tests and long-term cycling could be the more ordered structure for NTO-48h as described in Section 3.1. Therefore, NTO-48h would display more resilience to the sodium-ion insertion/extraction phenomena than NTO-8h.

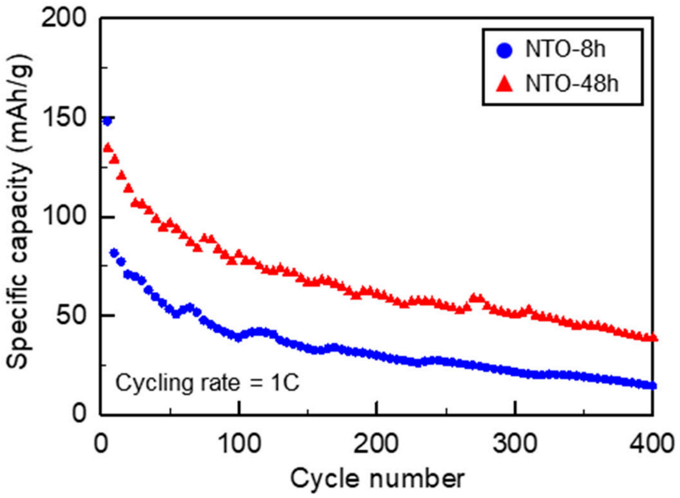

Figure 6. Electrochemical cycling at 1C rate during 400 cycles of NTO-8h and NTO-48h. Voltage window: 0.05-1.5 V *vs* Na+/Na.

3.4.3. Study of the Reaction Mechanism by Operando XRD

To better understand the improved electrochemical performance of NTO-48h in comparison to NTO-8h, both electrode materials were investigated by *operando* XRD during two first electrochemical cycles (Figure 7, Figure S3, and Figure S4). The evolution of the XRD patterns with cycling at a C/20 rate is shown in Figure S3 and Figure S4, where each diffractogram was recorded for one hour. The evolution of the sodium insertion into the NTO materials is summarized in Figure 7.

For both samples, no change appeared during the 25 first diffractograms (up to 0.2 V) (Figure 7). This result was expected as the first discharge plateau at around 0.6 V corresponds, as already mentioned, to the SEI formation during the first discharge and to the side reactions with carbon black. The peaks were indexed by $Na_2Ti_3O_7$, and by Be and BeO, which correspond to the cell contribution (Figure S3 and Figure S4).

Then, the sodium insertion into NTO material started at 0.2 V (27 h for NTO-8h and NTO-48h). To set the cycling rate at C/20, a current is applied in a defined voltage window such as, theoretically, the (dis)charge duration should take 20 hours. However, in practice, the charge and discharge time can be more or less than 20 hours, due to side reactions (such as SEI formation and the intercalation of Na^+ ions only in part of the material, respectively), and additional peaks gradually appear in the XRD patterns at 16° 2θ, 25° 2θ, 27.8° 2θ and 35.5° 2θ. At 0.1 V (30 h for NTO-8h and 32 h for NTO-48h), two supplementary peaks were gradually visible at 23.6° 2θ and 39.5° 2θ. This indicates a two-step sodium insertion, as described in the literature by several groups [13,15,16]. Moreover, this also corresponds to the study of Rudula *et al.* [21], who reported an *ex situ* XRD analysis of NTO material discharged to various potentials. The first series of peaks was attributed to the partially discharged material $Na_{4-x}Ti_3O_7$ (purple arrows in Figure S3 and Figure S4) and the second one to the fully discharged $Na_4Ti_3O_7$ material (green arrows in Figure S3 and Figure S4). The evolution of the peak intensities with the potential is qualitatively depicted by the gradually colored rectangles in Figure 7, where discharge and charge data are traced in black and in blue, respectively.

During the first charge, in NTO-8h and NTO-48h, the intermediate phase $Na_{4-x}Ti_3O_7$ disappeared step by step. However, regarding the fully discharged phase $Na_4Ti_3O_7$, a major difference emerged between two NTO materials. If the corresponding XRD peaks disappeared in NTO-48h at the end of the charge process, $Na_4Ti_3O_7$ remained present even at the end of the charge for NTO-8h. This result indicates that Na^+ ions were not fully extracted from the NTO-8h structure during the first charge. Some irreversibility in Na^+ extraction was also reported in the literature [13,15].

Examining the second discharge, the Na^+ ions were well intercalated in the NTO materials. Indeed, the intensity of the $Na_4Ti_3O_7$ XRD peaks gradually increased from 0.2 V for NTO-8h and NTO-48h. Nevertheless, the peaks of $Na_{4-x}Ti_3O_7$ did not appear as in the first discharge, neither for NTO-8h nor NTO-48h. This is coherent with the study of Rudola *et al.* [21], who reported the loss of the $Na_2Ti_3O_7 \rightarrow Na_{3-x}Ti_3O_7$ pathway in favor of the direct reaction $Na_2Ti_3O_7 \rightarrow Na_4Ti_3O_7$.

During the second charge, the same phenomenon as in the first charge occurred: the Na^+ ions were not completely extracted from NTO-8h structure, whereas the fully extracted $Na_2Ti_3O_7$ material is recovered for NTO-48h.

The *operando* XRD data were further analyzed by Rietveld refinement method. The lattice parameters were not evaluated during charge/discharge. The calculation of the Site Occupation Factors (SOF) for sites Na1 and Na2 (see Na1 and Na2 sites in Section 3.1) was also performed. However, because of the low resolution of the *operando* XRD data, getting accurate values was difficult and overcame the frame of this study. Therefore, SOF values were used to get qualitative information. The SOF evolution was plotted versus time using the *operando* electrochemical measurements (Figure S5). The NTO-8h material displayed nearly no variation in SOF. The most probable reason for this is that the Na^+ ions are trapped into the NTO structure during the charge. By contrast, SOF of the NTO-48h material exhibited much more changes, related to the total insertion and extraction of the additional Na^+ ions observed for this material.

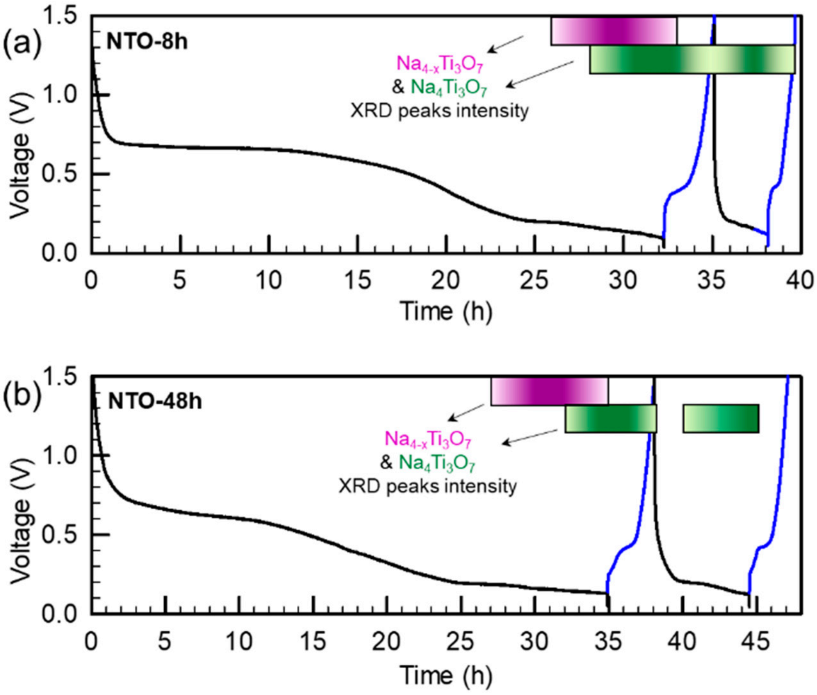

Figure 7. *In situ* XRD during electrochemical cycling of $Na_2Ti_3O_7$ synthesized by spray-drying following by a heat treatment at 800 °C during (a) 8 h and (b) 48 h. Voltage window: 0.05-1.5 V *vs* Na^+/Na; black curve corresponds to the discharge and blue curve to the charge. Each diffractogram was recorded in one hour and the cycling rate was set at C/20. Colored purple and green gradient rectangles depict $Na_{4-x}Ti_3O_7$ and $Na_4Ti_3O_7$ presence, respectively, based on the intensity of XRD peaks visible in Figure S3 and Figure S4.

3.4.4. Electrochemical Impedance Spectroscopy (EIS) Studies

Electrochemical impedance spectroscopy is a powerful and widely used non-destructive method used for the characterization of alkali-ion batteries and study the kinetics and electrochemical reaction mechanisms. In batteries, the ionic conduction in the electrolyte solution and electronic conduction through the particles may cause ohmic losses, as such the different contributions to the ohmic loss must be investigated. In this work, we carried out EIS measurements to compare the SEI and charge transfer resistance evolution in NTO-8h and NTO-48 electrodes, as well as to investigate the reasons for capacity fading upon cycling.

EIS tests for NTO-8h and NTO-48h at different voltage steps in the first two cycles were conducted. The impedance spectra at OCV (Figure 8a) include a high frequency semicircle with a loop at the medium frequency and an inclined line in the low-frequency region illustrating a capacitive behavior in the cell. This relates to the blocking character of the electrode at equilibrium potential due to the large charge transfer resistance coupled with double-layer capacitance.

A closer look at the spectra in the inset of Figure 8a shows that the spectra go into the negative values for the real part of impedance which is physically not possible. This originates from the presence of the loop in the medium frequency region that influences the way the effect of the current passing through both double layer capacitance and charge transfer resistance appears in the impedance spectra. Using EIS, it is possible to unambiguously distinguish between resistance and capacitance in the system. The resistance of the system is independent of the frequency, but capacitance is inversely dependent on it [43]. As shown in Figure S6, the impedance ($|Z|$) evolution does not follow the inverse dependency as it should. As the frequency decreases $f_1 > f_2 > f_3$ the impedance response, $|Z_3| < |Z_1| < |Z_2|$ only increases up to the second point at 120 Hz and then decreases at 2 Hz. Before further analysing the loop, we clarified that this feature is not a measurement artifact and checked the EIS data accuracy and validity. The easiest way to check this was to perform Kramers-Kroning test, a powerful tool to identify artifacts errors in a spectrum, which are mathematical relations for the real and imaginary components of a complex system that define it as linear, causal, stable, and finite. There is an excellent correlation between experimental results and the Kramers-Kronig fit with a χ^2 error statistic of only 0.003-0.005, showing no drift. As a result, the loop in the impedance spectra will have to be represented geometrically in the equivalent circuit.

The equivalent circuit used to fit the impedance response of NTO-8h and NTO-48h is shown in Figure 8f. R_s represents the internal resistance value of the bulk materials in a battery, such as the current collector, electrolyte, and separator. R_{SEI} and Q_{SEI} are resistance and constant phase element related to the SEI. R_{ct} and Q_{dl} are charge transfer resistance and constant phase element related to electric double-layer capacitance on active materials. $R_{L'}$, $R_{L''}$, Q_L and L are resistance, constant phase element, and inductance to represent an inductive loop geometrically but not a physical element. The origin of the inductive loop at low frequency has been a discussion point in literature and has mainly been related to the formation of passivation layers or the appearance of alkali ion-rich and poor regions [44]. The complete results of the equivalent circuit fitting illustrated by Nyquist plots for the NTO-8h in the first and second cycle, as well as NTO-48h in first and second cycle, are represented in Figure S7, Figure S8, Figure S9 and Figure S10, respectively.

The comparison between the impedance response at OCV and at 0.4V and 0.5V for NTO-8h and NTO-48h, respectively, show that the inclined line resulted from the blocking character of the electrode at OCV is bending toward the real impedance axis and forms a semicircle as the charge transfer resistance coupled with double layer capacitance is slightly decreased. The sluggish motion of electrons within the pristine materials results in the charge transfer resistance to remain very large (>848 Ω) for both NTO-8h and NTO-48h electrodes. The change in the form of the impedance spectra is more apparent at 0.2V in discharge where the appearance of the $Na_{4-x}Ti_3O_7$ phase was evidenced by XRD measurements (Figure 7). In the first discharge and upon sodiation of $Na_2Ti_3O_7$, the Ti^{4+} states in NTO materials are gradually transformed into the more electronically conductive Ti^{3+}/Ti^{4+} mixed valence states in $Na_{4-x}Ti_3O_7$ and $Na_4Ti_3O_7$ [45]. As such, the overall electronic conductivity increases, and charge transfer resistance substantially decreases at 0.2 V in discharge as manifested in Figure 8g-h. The charge transfer resistance decrease is more significant in NTO-48h that translates to improved performance and higher capacity. The charge transfer resistance however increases in both NTO-8h and NTO-48h at 0.1 V, due to the formation of $Na_4Ti_3O_7$ phase. As mentioned earlier the Na atoms are localized in two types of crystallographic sites in the NTO material so the insertion of Na^+ and formation of $Na_4Ti_3O_7$ phase in the first cycle results in charge transfer build up. $Na_4Ti_3O_7$ remained present even at the end of the charge for NTO 8h where nearly no variation in SOF for Na1 and Na2 was observed. The Na^+ ions that are trapped into the NTO structure during the charge step result in a huge increase in charge transfer resistance as shown in Figure 8. The Nyquist plot at the end of the charge shows large charge transfer resistance coupled with double-layer capacitance for both NTO-8h and NTO-48h. However, the charge transfer resistance at the initial stage of discharge for the second cycle in considerably lower in NTO-48h since the Na^+ ions could be extracted easily and the $Na_4Ti_3O_7$ phase is no longer present.

In addition to the changes in charge transfer resistance in the kinetically controlled impedance region, the Na^+ ion diffusion in the low frequency in the mass transport-controlled region is dominant and shows the most changes in resistive and capacitive behaviors. Figure S11, shows the Bode plots of the NTO-8h and NTO-48h electrodes at different discharge and charge steps in the first cycle. The phase angle as a function of frequency can be used to visualize the relative contributions of capacitive and resistive elements, with ideal capacitance at $\varphi = -90°$, and resistive processes indicated by $\varphi = 0$. The phase angle in the beginning of discharge and end of charge suggests a capacitive behavior and a resistive behavior with improved conduction of electrons across and through the electrode as well as less diffusion limitations in other parts of charge and discharge.

The characteristics of the SEI layer were also studied at different states of charge/discharge for both NTO-8h and NTO-48h. The fitted data show R_{SEI} of 19.8 Ω and 10.58 Ω for NTO-8h and NTO-48h, respectively. The resistive preliminary SEI of NTO-48h is transformed into a more conductive SEI layer at 0.1 V in discharge. At the end of discharge at 0.05 V, R_{SEI} for NTO-8h is 24.5 Ω which is higher than

doi:10.20944/preprints202308.0060.v1

7.4 Ω for the NTO-48h. This highlights the difference in the thickness and characteristics of the SEI layer in NTO-8h and NTO-48h. The evolution of the SEI resistance in the first charge step and the second cycle in NTO-48h, as well as the increase in R_s, suggest additional electrolyte consumption and decomposition resulting in capacity fading over long-term cycling as shown in Figure 6.

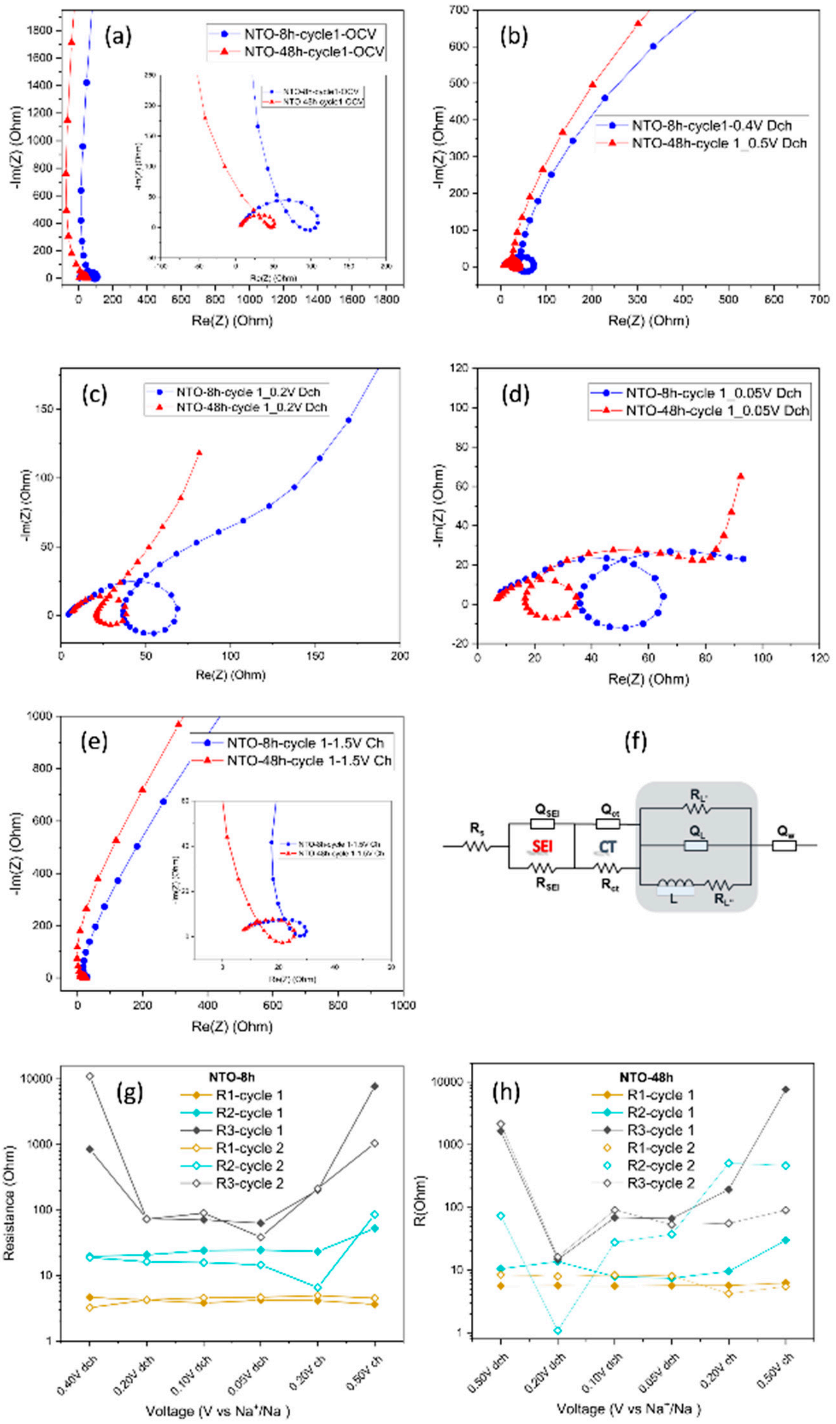

Figure 8. EIS tests of NTO-8h and NTO-48h electrodes with the Nyquist plots at: (a) OCV, (b) end of the first discharge plateau at 0.4V and 0.5V for NTO-8h and NTO-48h, respectively. Nyquist plots at (c) 0.2V in discharge, (d) 0.05V in discharge and (e) 1.5V at full charge. (f) Equivalent circuit used to fit the impedance response of NTO-8h and NTO-48h. The evolution of different resistance elements in the first and second cycles in (g) NTO-8h and NTO-48h.

4. Conclusion

In this work, new insights of the heat treatment effect on the electrochemical properties of NTO anode material were presented for the first time. Indeed, we showed that the heat treatment duration affects more the distortion of framework TiO_6 polyhedra than the extra-framework NaO_x polyhedra. Moreover, NTO-48h displays a more ordered structure than NTO-8h. By contrast, both materials exhibited similar morphology and the same oxidation state of titanium (Ti^{+4}), but NTO-48h sample displayed a lower specific surface area and lower surface contaminations determined by BET and XPS measurements, respectively.

The NTO-8h and NTO-48h materials were studied as anode materials for Na-ion batteries in half-cell configuration. The heat treatment duration influences drastically the electrochemical behaviour and performance. The delivered capacities are higher for NTO-48h than for NTO-8h. The peak voltage varied less in the cyclic voltammograms for NTO-48h, indicating more stability compared to NTO-8h. This observation was coherent with the Rietveld refinement on the pristine material, which showed an ordered structure for NTO-48h, leading to a more resilient insertion/extraction of Na^+ ions compound than NTO-8h.

The investigation of the reaction mechanism during discharge/charge processes by *operando* XRD evidenced that sodium insertion involves two phases, $Na_{4-x}Ti_3O_7$ and $Na_4Ti_3O_7$, during the first discharge. In the second cycle, only $Na_4Ti_3O_7$ was observed. For NTO-8h the sodium extraction was incomplete, whereas for NTO-48h-the $Na_2Ti_3O_7$ material was recovered. This Na^+ partial extraction from the NTO-8h structure should be the main reason for the lower capacities delivered by NTO-8h, compared to NTO-48h.

The electrochemical impedance spectroscopy tests showed lower SEI resistance at the end of the first discharge for NTO-48h. The evolution of SEI in the charge step and the second cycle shows a more stable SEI layer for NTO-8h which could be due to the preservation of the $Na_4Ti_3O_7$ phase. However, the charge transfer changes suggested a better performance and lower charge transfer resistance when the $Na_4Ti_3O_7$ phase formation was reversible upon cycling.

Supplementary Materials: The following supporting information can be downloaded at the website of this paper posted on Preprints.org. Electronic Supplementary Information (ESI) available: Rietveld refinement results and Experimental details of the X-ray powder diffraction pattern of NTO-8h and NTO-48h; *operando* XRD patterns and site occupation factor for sodium.

Acknowledgments: Electron microscopy was carried out at the CAREM platform (University of Liège). The authors are grateful to the University of Liège and FRS-FNRS for equipment grants. Region Ile-de-France is also acknowledged for partial support for the XPS equipment (Chimie ParisTech - CNRS, PSL University, Institut de Recherche de Chimie Paris).

References

[1] K. Chayambuka, G. Mulder, D.L. Danilov, P.H.L. Notten, Sodium-Ion Battery Materials and Electrochemical Properties Reviewed, Adv. Energy Mater. 8 (2018) 1–49. https://doi.org/10.1002/aenm.201800079.

[2] P. Senguttuvan, G. Rousse, V. Seznec, J.-M. Tarascon, M.R. Palacin, $Na_2Ti_3O_7$: Lowest Voltage Ever Reported Oxide Insertion Electrode for Sodium Ion Batteries, Chem. Mater. 23 (2011) 4109–4111. https://doi.org/10.1021/cm202076g.

[3] T. Perveen, M. Siddiq, N. Shahzad, R. Ihsan, A. Ahmad, M.I. Shahzad, Prospects in anode materials for sodium ion batteries - A review, Renew. Sustain. Energy Rev. 119 (2020) 109549. https://doi.org/10.1016/j.rser.2019.109549.

[4] J.-Y. Hwang, S.-T. Myung, Y.-K. Sun, Sodium-ion batteries: present and future, Chem. Soc. Rev. 46 (2017) 3529–3614. https://doi.org/10.1039/C6CS00776G.

[5] I. Hasa, S. Mariyappan, D. Saurel, P. Adelhelm, A.Y. Koposov, C. Masquelier, L. Croguennec, M. Casas-Cabanas, Challenges of today for Na-based batteries of the future: From materials to cell metrics, J. Power Sources. 482 (2021) 228872. https://doi.org/10.1016/j.jpowsour.2020.228872.

[6] Y. Zhen, Y. Chen, F. Li, Z. Guo, Z. Hong, M.M. Titirici, Ultrafast synthesis of hard carbon anodes for sodium-ion batteries, Proc. Natl. Acad. Sci. U. S. A. 118 (2021) 1–7. https://doi.org/10.1073/pnas.2111119118.

[7] K. Du, A. Rudola, P. Balaya, Investigations of Thermal Stability and Solid Electrolyte Interphase on $Na_2Ti_3O_7$/C as a Non-carbonaceous Anode Material for Sodium Storage Using Non-flammable Ether-based Electrolyte, ACS Appl. Mater. Interfaces. 13 (2021) 11732–11740. https://doi.org/10.1021/acsami.0c18670.

[8] Z. Hong, M. Kang, X. Chen, K. Zhou, Z. Huang, M. Wei, Synthesis of Mesoporous Co^{2+}-Doped TiO_2 Nanodisks Derived from Metal Organic Frameworks with Improved Sodium Storage Performance, ACS Appl. Mater. Interfaces. 9 (2017) 32071–32079. https://doi.org/10.1021/acsami.7b06290.

[9] H. Zhai, B.Y. Xia, H.S. Park, Ti-based electrode materials for electrochemical sodium ion storage and removal, J. Mater. Chem. A. 7 (2019) 22163–22188. https://doi.org/10.1039/c9ta06713b.

[10] J. Xia, H. Zhao, W.K. Pang, Z. Yin, B. Zhou, G. He, Z. Guo, Y. Du, Lanthanide doping induced electrochemical enhancement of $Na_2Ti_3O_7$ anodes for sodium-ion batteries, Chem. Sci. 9 (2018) 3421–3425. https://doi.org/10.1039/c7sc05185a.

[11] J. Nava-Avendaño, A. Morales-García, A. Ponrouch, G. Rousse, C. Frontera, P. Senguttuvan, J.-M. Tarascon, M.E. Arroyo-de Dompablo, M.R. Palacín, Taking steps forward in understanding the electrochemical behavior of $Na_2Ti_3O_7$, J. Mater. Chem. A. 3 (2015) 22280–22286. https://doi.org/10.1039/C5TA05174F.

[12] M. Zarrabeitia, F. Nobili, M.A. Munoz-Marquez, T. Rojo, M. Casas-Cabanas, Direct observation of electronic conductivity transitions and solid electrolyte interphase stability of $Na_2Ti_3O_7$ electrodes for Na-ion batteries, J. Power Sources. 330 (2016) 78–83. https://doi.org/10.1016/j.jpowsour.2016.08.112.

[13] T.L. Kulova, Y.O. Kudryashova, A.A. Kuz'mina, I.A. Stenina, A.A. Chekannikov, A.B. Yaroslavtsev, J. Libich, Study of degradation of $Na_2Ti_3O_7$-based electrode during cycling, J. Solid State Electrochem. 23 (2019) 455–463. https://doi.org/10.1007/s10008-018-4154-1.

[14] W. Wang, C. Yu, Y. Liu, J. Hou, H. Zhu, S. Jiao, Single crystalline $Na_2Ti_3O_7$ rods as an anode material for sodium-ion batteries, RSC Adv. 3 (2013) 1041. https://doi.org/10.1039/c2ra22050d.

[15] A. Rudola, K. Saravanan, C.W. Mason, P. Balaya, $Na_2Ti_3O_7$: an intercalation based anode for sodium-ion battery applications, J. Mater. Chem. A. 1 (2013) 2653–2662. https://doi.org/10.1039/C2TA01057G.

[16] H. Pan, L. Xia, X. Yu, Y.-S. Hu, H. Li, X.-Q. Yang, L. Chen, Sodium Storage and Transport Properties in Layered $Na_2Ti_3O_7$ for Room-Temperature Sodium-Ion Batteries Sodium, Adv. Energy Mater. 3 (2013) 1186–1194. https://doi.org/10.1002/aenm.201300139.

[17] J. Xu, C. Ma, M. Balasubramanian, Y. Shirley, Understanding $Na_2Ti_3O_7$ as an ultra-low voltage anode material for a Na-ion battery, Chem. Commun. 50 (2014) 12564–12567.

https://doi.org/10.1039/C4CC03973D.

[18] W. Zou, J. Li, Q. Deng, J. Xue, X. Dai, A. Zhou, J. Li, Microspherical Na2Ti3O7 prepared by spray-drying method as anode material for sodium-ion battery, Solid State Ionics. 262 (2014) 192–196. https://doi.org/10.1016/j.ssi.2013.11.005.

[19] S. Wen, X. Li, J. Zhang, J. Wang, H. Ding, N. Zhang, D. Zhao, L. Mao, S. Li, Effects of sodium salts on compatibility between $Na_2Ti_3O_7$@C anode and electrolyte for sodium-ion batteries, J. Alloys Compd. 930 (2023) 167380. https://doi.org/10.1016/j.jallcom.2022.167380.

[20] Y. Li, Y. Liu, D. Wang, C. Hu, K. Luo, B. Zhong, Y. Sun, Y. Liu, Z. Wu, X. Guo, Enabling both ultrahigh initial coulombic efficiency and superior stability of $Na_2Ti_3O_7$ anodes by optimizing binders, J. Mater. Chem. A. 10 (2022) 24178–24189. https://doi.org/10.1039/d2ta07097a.

[21] A. Rudola, N. Sharma, P. Balaya, Introducing a 0.2 v sodium-ion battery anode: The $Na_2Ti_3O_7$ to $Na_{3-x}Ti_3O_7$ pathway, Electrochem. Commun. 61 (2015) 10–13. https://doi.org/10.1016/j.elecom.2015.09.016.

[22] S. Papp, L. Korosi, V. Meynen, P. Cool, E.F. Vansant, I. Dekany, The influence of temperature on the structural behaviour of sodium tri- and hexa-titanates and their protonated forms, J. Solid State Chem. 178 (2005) 1614–1619. https://doi.org/10.1016/j.jssc.2005.03.001.

[23] Y.C. Pak, C.H. Rim, S.G. Hwang, K.C. Ri, C.J. Yu, Defect formation and ambivalent effects on electrochemical performance in layered sodium titanate $Na_2Ti_3O_7$, Phys. Chem. Chem. Phys. (2023) 3420–3431. https://doi.org/10.1039/d2cp05403e.

[24] Y.S. Choi, S.I.R. Costa, N. Tapia-Ruiz, D.O. Scanlon, Intrinsic Defects and Their Role in the Phase Transition of Na-Ion Anode $Na_2Ti_3O_7$, ACS Appl. Energy Mater. 6 (2023) 484–495. https://doi.org/10.1021/acsaem.2c03466.

[25] Y. Cao, Q. Ye, F. Wang, X. Fan, L. Hu, F. Wang, T. Zhai, H. Li, A New Triclinic Phase $Na_2Ti_3O_7$ Anode for Sodium-Ion Battery, Adv. Funct. Mater. 30 (2020) 2003733. https://doi.org/10.1002/adfm.202003733.

[26] C. Piffet, B. Vertruyen, F. Hatert, R. Cloots, F. Boschini, A. Mahmoud, High temperature X-ray diffraction study of the formation of $Na_2Ti_3O_7$ from a mixture of sodium carbonate and titanium oxide, J. Energy Chem. 65 (2022) 210–218. https://doi.org/10.1016/j.jechem.2021.05.050.

[27] S.D.S. Costa, Juliana Pereira da Silva, Matheus Moraes Biondo, E.A. Sanches, M.M.D.S. Paula, F.X. Nobre, J.A. Rivera, Y.A. Zulueta, M.S. Torikachvili, D.V. Sampaio, M.V.D. Vermelho, S. Tălu, L.A. Dominguez, Y. Leyet, Temperature Dependence of the Electrical Properties of $Na_2Ti_3O_7$/$Na_2Ti_6O_{13}$/POMA Composites, Molecules. 27 (2022) 5756. https://doi.org/10.3390/molecules27185756.

[28] O. V Yakubovich, V. V Kireev, Refinement of the crystal structure of $Na_2Ti_3O_7$, Crystallogr. Reports. 48 (2003) 24–28. https://doi.org/10.1134/1.1541737.

[29] J. Rouquerol, P. Llewellyn, F. Rouquerol, Is the BET equation applicable to microporous adsorbents?, Stud. Surf. Sci. Catal. 160 (2007) 49–56. https://doi.org/10.1016/s0167-2991(07)80008-5.

[30] J.B. Leriche, S. Hamelet, J. Shu, M. Morcrette, C. Masquelier, G. Ouvrard, M. Zerrouki, P. Soudan, S. Belin, E. Elkaïm, F. Baudelet, An Electrochemical Cell for Operando Study of Lithium Batteries Using

Synchrotron Radiation, J. Electrochem. Soc. 157 (2010) A606. https://doi.org/10.1149/1.3355977.

[31] S. Andersson, A.D. Wadsley, The crystal structure of $Na_2Ti_3O_7$, Acta Crystallogr. 14 (1961) 1245–1249. https://doi.org/10.1107/s0365110x61003636.

[32] I. D. Brown, D. Altermatt, Bond-valence parameters obtained from a systematic analysis of the Inorganic Crystal Structure Database, Acta Crystallogr. Sect. B. 41 (1985) 244–247. https://doi.org/10.1107/S0108768185002063.

[33] C. Gadois, J. Światowska, S. Zanna, P. Marcus, Influence of titanium surface treatment on adsorption of primary amines, J. Phys. Chem. C. 117 (2013) 1297–1307. https://doi.org/10.1021/jp306786w.

[34] J. Ma, W. Li, B.J. Morgan, J. Światowska, R. Baddour-Hadjean, M. Body, C. Legein, O.J. Borkiewicz, S. Leclerc, H. Groult, F. Lantelme, C. Laberty-Robert, D. Dambournet, Lithium Intercalation in Anatase Titanium Vacancies and the Role of Local Anionic Environment, Chem. Mater. 30 (2018) 3078–3089. https://doi.org/10.1021/acs.chemmater.8b00925.

[35] S. Mehraz, W. Luo, J. Swiatowska, B. Bezzazi, A. Taleb, Hydrothermal synthesis of TiO_2 aggregates and their application as negative electrodes for lithium-ion batteries: The conflicting effects of specific surface and pore size, Materials (Basel). 14 (2021) 1–15. https://doi.org/10.3390/ma14040916.

[36] T. Song, S. Ye, H. Liu, Y.G. Wang, Self-doping of Ti3^{+i} nto $Na_2Ti_3O_7$ increases both ion and electron conductivity as a high-performance anode material for sodium-ion batteries, J. Alloys Compd. 767 (2018) 820–828. https://doi.org/10.1016/j.jallcom.2018.07.186.

[37] M.A. Muñoz-Márquez, M. Zarrabeitia, E. Castillo-Martínez, A. Eguía-Barrio, T. Rojo, M. Casas-Cabanas, Composition and Evolution of the Solid-Electrolyte Interphase in $Na_2Ti_3O_7$ Electrodes for Na-Ion Batteries: XPS and Auger Parameter Analysis, ACS Appl. Mater. Interfaces. 7 (2015) 7801–7808. https://doi.org/10.1021/acsami.5b01375.

[38] C. D. Wanger, W.M. Riggs, L.E. Davis, J.F. Moulder, G.E. Muilenberg, Handbook of X-ray Photoelectron Spectroscopy, Perkin-Elmer Corp., Physical Electronics Division: Eden Praire, 1979. https://doi.org/10.1002/sia.740030412.

[39] H.S. Bhardwaj, T. Ramireddy, A. Pradeep, M.K. Jangid, V. Srihari, H.K. Poswal, A. Mukhopadhyay, Understanding the Cyclic (In)stability and the Effects of Presence of a Stable Conducting Network on the Electrochemical Performances of $Na_2Ti_3O_7$, ChemElectroChem. 5 (2018) 1219–1229. https://doi.org/10.1002/celc.201701276.

[40] A. Mukherjee, D. Das, S. Banerjee, S.B. Majumder, Synthesis and electrochemical performance of in-situ and ex-situ carbon-coated $Na_2Ti_3O_7$, as a promising anode for sodium-ion batteries, Electrochem. Sci. Adv. (2022) e2100118. https://doi.org/10.1002/elsa.202100118.

[41] T.L. Kulova, A.M. Skundin, Balance between reversible and irreversible processes during lithium intercalation in graphite, Russ. J. Electrochem. 42 (2006) 251–258. https://doi.org/10.1134/S1023193506030074.

[42] A. Mahmoud, J.M. Amarilla, K. Lasri, I. Saadoune, Influence of the synthesis method on the electrochemical properties of the $Li_4Ti_5O_{12}$ spinel in Li-half and Li-ion full-cells. A systematic

comparison, Electrochim. Acta. 93 (2013) 163–172. https://doi.org/10.1016/j.electacta.2013.01.083.

[43] N.O. Laschuk, E.B. Easton, O. V. Zenkina, Reducing the resistance for the use of electrochemical impedance spectroscopy analysis in materials chemistry, RSC Adv. 11 (2021) 27925–27936. https://doi.org/10.1039/d1ra03785d.

[44] D. Klotz, Negative capacitance or inductive loop? – A general assessment of a common low frequency impedance feature, Electrochem. Commun. 98 (2019) 58–62. https://doi.org/10.1016/j.elecom.2018.11.017.

[45] Y. Zhang, Y. Tang, J. Deng, W.R. Leow, H. Xia, Z. Zhu, Z. Lv, J. Wei, W. Li, C. Persson, O.I. Malyi, M. Antonietti, X. Chen, Correlating the Peukert's Constant with Phase Composition of Electrode Materials in Fast Lithiation Processes, ACS Mater. Lett. 1 (2019) 519–525. https://doi.org/10.1021/acsmaterialslett.9b00320.